



Investigation of the mechanisms of Type-II hot corrosion of superalloy CMSX-4



Pongpat Lortrakul, Rodney W. Trice*, Kevin P. Trumble, Mysore A. Dayananda

Purdue University, School of Materials Engineering, 701 West Stadium Avenue, West Lafayette, IN 47907, United States

ARTICLE INFO

Article history:

Received 6 June 2013

Accepted 29 November 2013

Available online 4 December 2013

Keywords:

A. Superalloys
C. Hot corrosion
C. Oxidation
C. Sulfidation

ABSTRACT

A microstructural investigation of Type-II hot corrosion was carried out on a single crystal Ni-based superalloy (CMSX-4) pre-coated with Na_2SO_4 at 700 °C in a flowing $\text{O}_2\text{-SO}_2\text{-SO}_3$ atmosphere. Corrosion occurred by rapid dissolution of the alloy by molten sulfate eutectics, forming an outer layer rich in Co and Ni and an inner layer rich in Cr and Al. The outer layer transformed into mixed oxides of Co and Ni, with concurrent evolution of the continuous S-rich inner layer. A multicomponent analysis provides insight into diffusional interactions among Co, Ni, and S. Crystal orientation and microstructure effects were also studied.

© 2013 Elsevier Ltd. All rights reserved.

1. Introduction

Uncoated areas of gas turbine blades, such as below the platform, can experience significant hot corrosion [1] in the presence of sodium sulfate (Na_2SO_4) [2,3] at temperatures as low as ~700 °C, particularly in marine applications. In this temperature range pits can form in the alloy, creating localized high stresses under service loading. Cracks can initiate and propagate from these pits, causing premature failure [4]. Hot corrosion occurs on Ni- and Co-based superalloys, as well as on their Cr- and Al-rich coating alloys, and under a range of different conditions [5–13].

There are two temperature-dependent regimes of Na_2SO_4 hot corrosion as observed by peaks in corrosion rate, which are more aggressive than in air exposure alone. These two corrosion rate peaks occur at ~900–1000 °C (Type-I) and ~600–750 °C (Type-II). Type-I hot corrosion is associated with melting of Na_2SO_4 ($T_m = 884$ °C) and its interaction with the surface. In Type-II hot corrosion, also known as low-temperature hot corrosion, molten eutectic $\text{Na}_2\text{SO}_4\text{-MSO}_4$ (where M is Ni or Co) forms that acts to degrade the surface. Type II corrosion does not proceed without a minimum SO_3 partial pressure [6]. The present study focuses exclusively on Type II hot corrosion at 700 °C.

Type II hot corrosion mechanisms have been described by Pettit and Meier [5,6] and Luthra [7,8]. Na_2SO_4 , which is applied to the surface, is a solid phase at 700 °C. With sufficient p_{SO_3} in the

atmosphere, sulfation of the NiO or CoO occurs to form NiSO_4 or CoSO_4 . The minimum SO_3 pressures to form NiSO_4 and CoSO_4 are approximately 2×10^{-4} and 2×10^{-5} atm, respectively [8,14,15]. Either compound will further react with excess Na_2SO_4 on the surface to form the eutectic liquid $\text{Na}_2\text{SO}_4\text{-MSO}_4$. The pure $\text{Na}_2\text{SO}_4\text{-CoSO}_4$ and $\text{Na}_2\text{SO}_4\text{-NiSO}_4$ liquid phases form at 576 °C [16,17] and 631 °C [18,19], respectively. Luthra [8] attributed the low-temperature corrosion of cobalt-based alloys to the rapid dissolution of cobalt oxides by the sulfate liquid, preventing the formation of protective Cr_2O_3 or Al_2O_3 .

An extensive search of the literature on Type II hot corrosion revealed that the studies of Luthra [7,8] remain the most definitive work on the general mechanisms [6]. Using model Co-Cr, Co-Al, and Co-Cr-Al alloys, Luthra [8] described the Type II corrosion mechanism in Co-alloys as occurring by inward transport of S through the $\text{Na}_2\text{SO}_4\text{-CoSO}_4$ liquid via $\text{S}_2\text{O}_7^{2-}$ generated at the molten sulfate surface by reaction with SO_3 gas and SO_4^{2-} . CoO dissolution in the molten salt and counter-diffusion of Co ions was proposed, with Co^{2+} moving outward and Co^{3+} inward. Although Al_2O_3 and Cr_2O_3 were predicted to be stable under the conditions studied, they were not observed and dissolution of the Co oxides (acidic fluxing) was proposed to prevent the formation of a protective $\text{Al}_2\text{O}_3/\text{Cr}_2\text{O}_3$ layer and sustain continuous attack.

Extending this mechanism to Ni-based alloys containing no Co, Luthra noted that comparatively little sulfation of NiO is predicted on thermodynamic grounds. Chiang, Pettit and Meier [5] proposed that in Ni-based alloys the sulfidation/oxidation of Al and Cr occurs under Type II conditions, although in general the transition from fluxing to stable sulfide/oxide formation is still not well

* Corresponding author. Address: Neil Armstrong Hall of Engineering, 701 West Stadium Avenue, West Lafayette, IN 47907, United States. Tel.: +1 765 494 6405; mobile: +1 765 418 4547.

E-mail address: rtrice@purdue.edu (R.W. Trice).

understood [6,20]. Other recent reviews [10,13] do not indicate any more detailed mechanistic studies on the Type II hot corrosion in the Ni-based alloys and point out [21] the “dearth” of open literature on effects of microstructure on Type II corrosion in general.

The majority of recent work (Type I or Type II) has been on Cr- and Al-rich coating alloys [21–28]. Most of the studies on γ/γ' superalloys, which contain lower Cr and Al concentrations than the coating alloys, have primarily focused on Type I behavior and not on microstructural mechanisms. An early study on the oxidation and hot corrosion of uncoated single crystal γ/γ' superalloys included limited investigation of Type II hot corrosion specimen on one of the alloys [29]. Whereas more recent work on single crystal alloys [30,31] has focused on Type I behavior and/or coated alloys, systematic studies of Type II hot corrosion on a single crystal nickel-based superalloy under well-defined conditions are lacking.

In the current study, an investigation of Type-II hot corrosion of the single crystal Ni-based superalloy CMSX-4 was conducted to examine the microstructural development of the corrosion scale. Oriented samples of an as-cast crystal were pre-coated with Na_2SO_4 and tested at 700 °C in a flowing, controlled $\text{O}_2\text{-SO}_2\text{-SO}_3$ atmosphere. The development of the corrosion scale and subscale microstructure was studied using scanning electron microscopy (SEM), energy dispersive spectroscopy (EDS) and X-ray diffraction (XRD).

2. Experimental procedure

All hot corrosion tests were performed on samples cut from a single 75 mm × 50 mm × 12 mm slab of as-cast CMSX-4 crystal produced by Alcoa Howmet Research Center, Whitehall, MI. The nominal composition of CMSX-4 (in wt.%) is: balance Ni, 9.0 Co, 6.5 Cr, 6.5 Ta, 6.4 W, 5.6 Al, 3.0 Re, 1.0 Ti, 0.6 Mo and 0.1 Hf. The slab was within the standard alloy specification, as confirmed by EDS analysis conducted at Purdue University. The alloy was intentionally used in the as-cast condition in order to study the effects of microstructural features, including fine and coarse γ' precipitates (~1 μm) interdendritic γ/γ' eutectic (~20–50 μm) and microporosity, as well as crystallographic orientation, on hot corrosion behavior. The crystallographic orientation of the slab was confirmed using a Bruker GADDS X-ray diffractometer. The results showed that the longitudinal slab axis (growth direction) varied less than 7° from the [001] direction and the transverse directions less than 4° from [100] and [010].

Hot corrosion specimens, 10 mm × 10 mm × 10 mm, were made by cutting with a low speed diamond saw. Specimens were prepared to examine hot corrosion on (100)=(010) surfaces (transverse to the dendrite growth axis) and on (001) surfaces (growth direction). All surfaces were fine-ground with 600 grit SiC paper, then degreased with acetone, rinsed in deionized water and dried at 150 °C. The Na_2SO_4 was applied by spraying a 0.7 wt.% Na_2SO_4 -water solution from a 25 cm distance onto the one surface of each sample being corroded. Details of this process are available in [32]. A dried salt layer of $0.3 \pm 0.03 \text{ mg/cm}^2$ was achieved via several 10-s sprays, and optical microscopy revealed a fine distribution of the salt on the sample surface. The estimated thickness of the applied salt layer was ~1.2 μm based on a Na_2SO_4 density of 2.66 g/cm³. Individual specimens were set in alumina dishes, placed in a 90 cm long tube furnace and heated to 700 ± 5 °C at a rate of 10 °C/min. A premixed gas of 1000 ppm SO_2 in O_2 was flowed into the furnace at 50 cc/min at 1 atm pressure. A honeycomb Pt catalyst was placed at the entrance of the furnace to accelerate the $\text{O}_2\text{-SO}_2\text{-SO}_3$ equilibrium condition, corresponding to $p_{\text{SO}_3} = 7.2 \times 10^{-4}$ atm, which was greater than the amount required to meet the minimum criteria

to create a Type-II hot corrosion environment for both Ni and Co [8,14].

Specimens were exposed at temperature for 3, 15, and 30 min, and 5 and 50 h, with a single salt application. Samples could not be removed from the furnace immediately after the testing time expired. Rather, the $\text{SO}_2\text{/O}_2$ gas flow was stopped and the furnace was turned off and allowed to cool naturally. Direct measurements of the cooling transient indicated that within 30 min the specimens cooled to ~600 °C, at which the relative rate of thermally activated processes would be negligible compared to 700 °C. It should be noted that the heating and cooling transients make the effective reaction time longer than the hold times, although this difference is systematic and a precise determination of the reaction kinetics was not the aim of this study.

Following testing, corrosion products on the surface of the samples were identified via XRD using a Bruker D8 Focus diffractometer. Samples were next mounted in a room-temperature curing epoxy, cross-sectioned, and polished using diamond abrasives and 0.3- μm alumina suspension in the final step. Kerosene was used as the carrier during polishing instead of water to prevent the loss of any water-soluble compounds in the scale. A final ultrasonic cleaning step in ethanol was used to remove polishing residue in the surface crevices. In some specimens the structure of the alloy was revealed by immersion etching with a solution of 33 vol.% deionized water, 33 vol.% acetic acid, 33 vol.% nitric acid, and 1 vol.% hydrofluoric acid for ~5 s. Microstructure and EDS analysis (point and area mapping) were performed on a Phillip FEI XL-40 SEM operated at 25 keV, with a thin-window detector for the standardized EDS analyses.

The volume fraction and size of the γ' precipitate structures were measured on SEM images using standard stereology techniques [33,34]. The area fraction (A_A) = volume fraction (V_V) and number of γ/γ' boundary intersections per unit length (P_L) were determined with Image-J (version 1.44p). From these measurements the precipitate size as mean intercept length ($L_3 = 2V_V/P_L$) was calculated.

3. Results

3.1. Scale development as a function of corrosion time

Cross-section micrographs of the scale development with time are shown in Fig. 1. A 3-min test was selected to examine the very early stages of hot corrosion (Fig. 1a), which resulted in a 1–2 μm thick corrosion scale, including any residual sodium sulfate. When the test duration was increased to 15 min two distinct layers were observed, identified as outer and inner layers, as shown in Fig. 1b. The corrosion scale, consisting of these two layers, increased with time as shown in Fig. 1c and d for samples tested for 5 h and 50 h, respectively. The scale produced after 50 h testing spalled off from the CMSX-4 during cooling and was mounted without the CMSX-4 substrate in Fig. 1d. A distinctive feature of the scale cross-sections is that the natural marker between the two layers is flat and sharp, in contrast to the free surface and substrate interface with the inner layer, especially at longer times.

Variations of the thicknesses of the inner and outer layers, as well as of the total corrosion scale as a function of time are presented in Fig. 2. The data plotted are the average and standard deviation of 50–100 systematic (equally spaced) measurements of the inner and outer layers, and overall scale thickness for each test condition. The outer layer was usually thicker than the inner layer. The growth of the scale exhibited approximate parabolic kinetics, but then slowed, most likely reflecting the limiting effect of the single salt application.

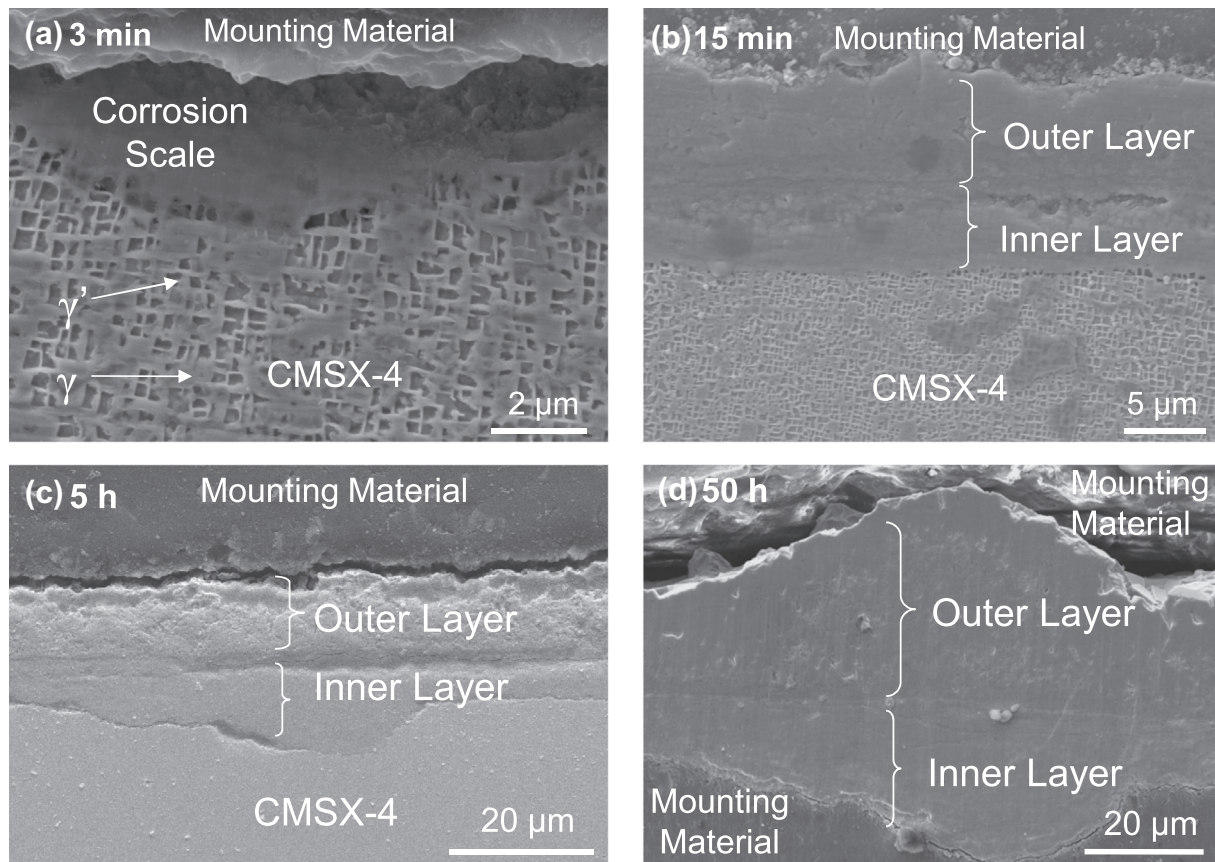


Fig. 1. SEM images showing the development of Type-II hot corrosion scale as a function of test time. Each sample was coated with $0.3 \text{ mg}/\text{cm}^2 \text{ Na}_2\text{SO}_4$ prior to heating to 700°C for (a) 3 min, (b) 15 min, (c) 5 h and (d) 50 h.

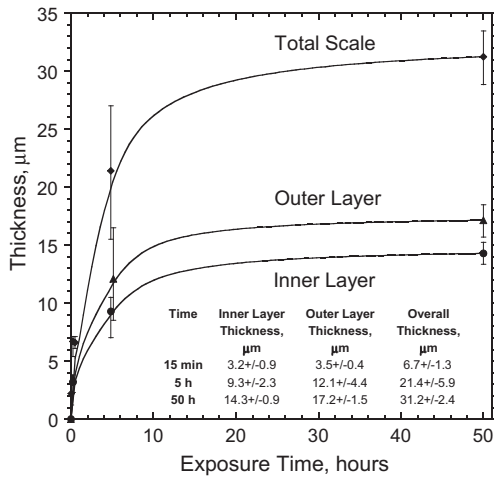


Fig. 2. A plot of scale thickness for CMSX-4 specimens tested in Type II hot corrosion versus exposure time. The inner and outer layers and total thickness of the scale are plotted. The data for 5 h are offset slightly in time for clarity.

3.2. Reaction products as a function of corrosion time

EDS mapping performed on the 3-min specimen shown in Fig. 1a did not compositionally distinguish the structure within the thin scale. The compositional distribution after 15- and 30-min tests (also not shown) were similar to the pattern in the 5 h test shown in Fig. 3, but the overall scale thickness in each was thinner. As shown in Fig. 3, a Co-rich layer was observed to develop

above a continuous Ni-rich layer as part of the outer layer. EDS maps of Cr and Al (see Fig. 3) indicated their distribution mainly in the inner layer.

A point-by-point EDS line analysis was conducted for Co, Ni, and S, beginning in the outer layer, through the inner layer and into the CMSX-4 alloy for a sample corroded for 5 h. These results are shown in Fig. 4, where x_0 represents the original uncorroded surface of the base alloy, x_I the interface between the outer and inner layers and x_{II} the interface between the inner layer and the base alloy. After 5 h of hot corrosion, x_0 , x_I and x_{II} were $8.9 \mu\text{m}$, $10.6 \mu\text{m}$, and $22.3 \mu\text{m}$, respectively. The concentration of Co, beginning in the original alloy at ~ 8 at.%, decreases in the inner layer and then rises significantly over the last $2-3 \mu\text{m}$ in the outer layer, consistent with the Co EDS map shown in Fig. 3. The concentration of Ni (Fig. 4b) decreases in the inner layer, but rises in the outer layer, before decreasing near the external surface. The S concentration profile after 5 h (Fig. 4c) exhibits a higher level in the inner layer than the outer layer, consistent with Fig. 5, as well as distinct S enrichment near the two interfaces.

When the exposure time was increased to 50 h, discrete Co-rich regions (see Fig. 5) replaced the continuous Co-rich layer observed after a 5 h test (Fig. 3). Like the EDS concentration plot for S after 5 h of hot corrosion (see Fig. 4c), the S is concentrated at the interfaces x_I and x_{II} , with less S found in the middle of the inner layer. Whereas, Cr and Al are localized in the inner layer, similar to the 5 h condition shown in Fig. 3.

XRD of the surfaces after hot corrosion was used to identify the various reaction products after 30 min, 5 h and 50 h testing. The results are presented in Fig. 6. After 30 min, Ni_2O_4 , a reaction product of Na_2SO_4 and NiO , was detected. NiO was also shown to be present

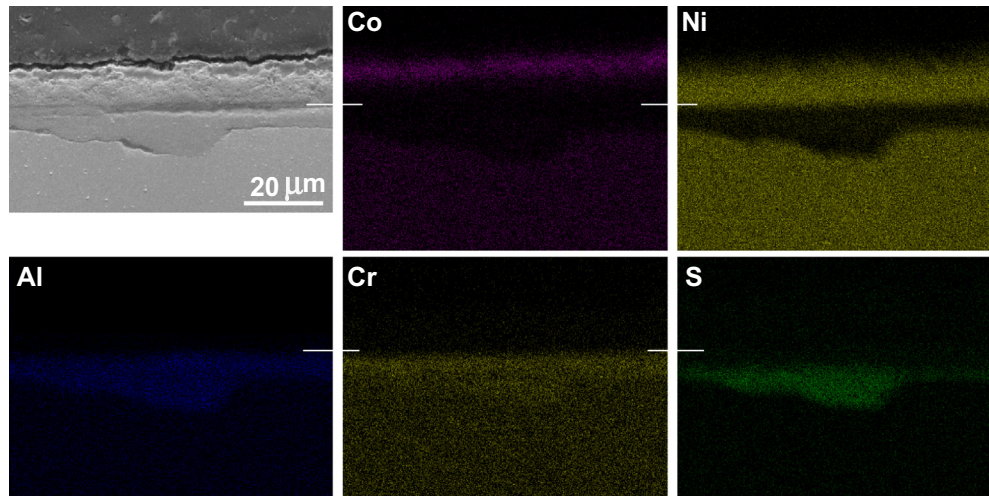


Fig. 3. SEM image of the scale after 5 h of Type II hot corrosion and the corresponding EDS maps for Co, Ni, Al, Cr, and S. The white line indicates the original surface.

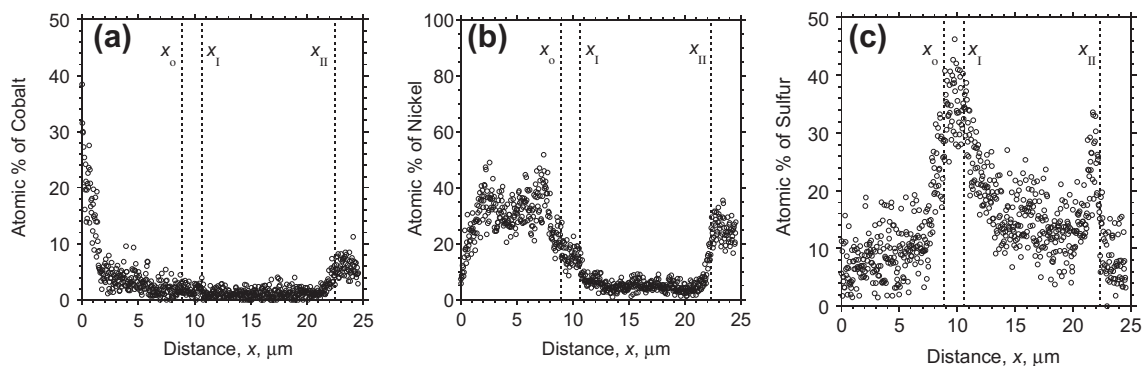


Fig. 4. EDS plots for (a) Co, (b) Ni and (c) S versus distance after 5 h of Type II hot corrosion. Zero distance represents the surface of the corroded specimen.

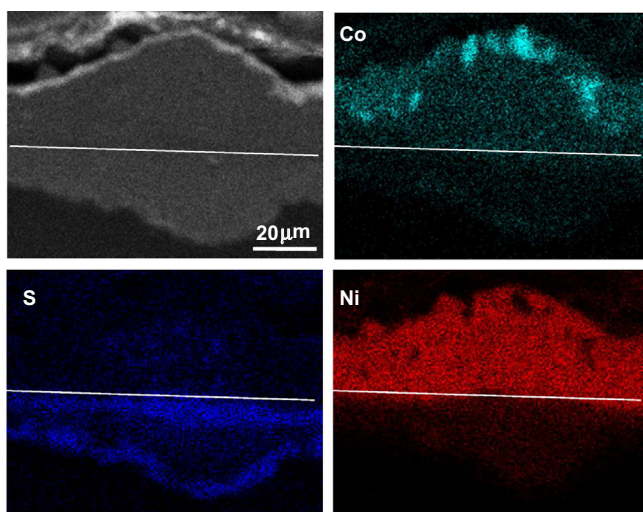


Fig. 5. SEM images of the scale after 50 h of Type II hot corrosion and the corresponding EDS maps for Co, S, and Ni. Not shown are the EDS maps for Al and Cr, which remained concentrated in the inner layer.

[35]. As shown in Fig. 6, after 5 h of testing the Na_2SO_4 disappeared and was replaced by CoO and NiO peaks. The CoO and NiO have the same crystal structure (NaCl-type) with lattice parameters of 0.426

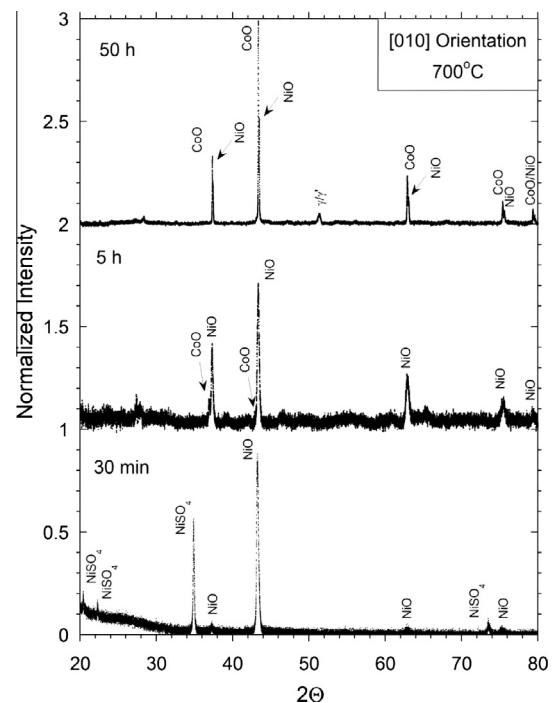


Fig. 6. X-ray diffraction results of the surface scale after 30 min, 5 h and 50 h of hot corrosion testing.

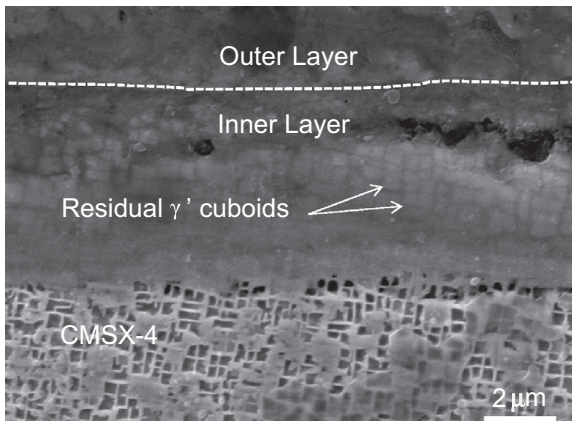


Fig. 7. SEM images after 15 min showing the presence of residual γ' cuboid structure in the inner layer and their progressive dissolution from the external surface.

and 0.418 nm, respectively. The diffraction peaks associated with CoO, with a slightly larger lattice parameter, always appear to the left of the NiO diffraction peaks in Fig. 6. For 5 h of hot corrosion testing, the CoO peaks were all less intense than the NiO peaks, and were shifted slightly to the right of their expected 2Θ positions. This suggests that the CoO contains some NiO as well. Indeed, CoO does have considerable solubility for NiO at 700 °C [36]. After 5 h of testing there were also numerous low-intensity peaks, most likely attributed to sulfides. However, CoS was the most likely peak identified [35]. A more detailed microscopy investigation such as transmission electron microscopy would be required to more precisely identify the compounds occurring for this testing condition.

The 50-h hot corrosion results are also shown in Fig. 6. The same closely spaced peaks from CoO and NiO as after 5 h are evident in the XRD spectra. However, the CoO peaks are now of greater intensity than the NiO peaks. No peaks associated with Ni or Co sulfides could be verified.

3.3. γ/γ' Microstructure after corrosion

Fig. 7 shows a polished and etched cross-section after 15 min of hot corrosion testing. The γ' cuboidal precipitate morphology is still partially visible within the inner layer of the scale. Similar observations were made for both the 5 h and the 50 h tests. The presence of the residual γ' cuboids in a region of the sample that has clearly been corroded indicates a slower corrosion rate for this phase compared to the γ matrix. Thus, the γ matrix, which is primarily composed of Ni, Co, and Cr, appears to be the first phase dissolved by the eutectic liquid. However, with further time the γ' cuboids also corrode completely. Microanalysis by EDS in the inner scale regions containing the residual γ' cuboids indicated high concentrations of W and Ta (~20 wt.%), although there is some uncertainty due to peak overlap for these elements.

3.4. Effect of CMSX-4 microstructure on hot corrosion

The characteristic dendritic structure of the as-cast CMSX-4 is shown in Fig. 8a. This surface is the (010) plane or side surface relative to crystal growth direction and plan view of the surfaces on which most of the corrosion tests were conducted. Prominent features are the eutectic γ/γ' pools, which form in the interdendritic regions in the last stage of local solidification. The occasional solidification shrinkage pore is also present in these regions. The interdendritic regions (region a in Fig. 8a) also exhibit coarser

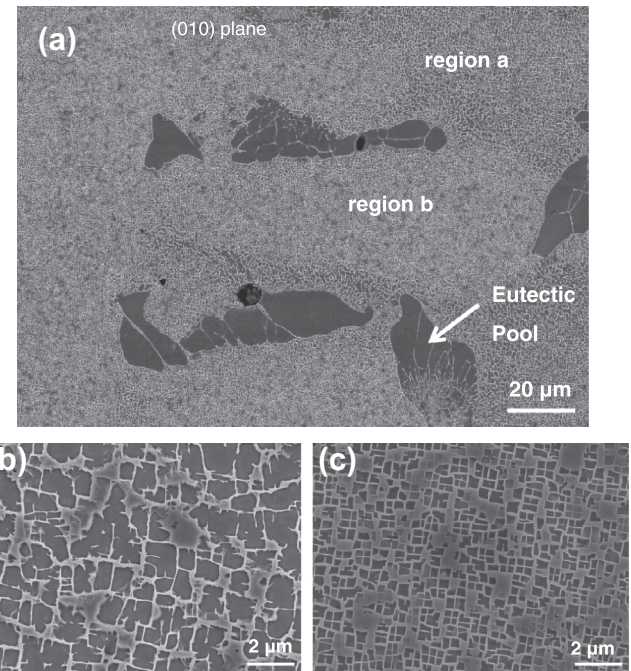


Fig. 8. (a) SEM micrograph of the CMSX-4 as-cast microstructure showing an interdendritic (region a) and dendrite core (region b). The surface was the (010) plane. Images (b and c) show higher magnifications of the interdendritic and dendrite core zones, respectively.

γ' precipitates, which form on cooling in the solid state, compared to the dendrite cores (region b). Fig. 8b and c are higher magnification images that compare the coarse and fine γ' precipitate structures. Quantitative microstructural analysis showed that both the size and volume fraction of the γ' precipitates were larger in the interdendritic regions, with mean intercept sizes (\bar{L}_3) of 1.28 ± 0.14 and 0.56 ± 0.05 and volume fractions (V_V) of 0.77 ± 0.01 and 0.65 ± 0.01 , respectively, compared to in the dendrite cores.

Elemental analysis by EDS (not shown) was used to detect differences in the distribution of alloying elements in the interdendritic and dendrite core regions. The Cr was nearly all depleted and the Co partially depleted in the interdendritic regions. However, the Ni, Al, Ta, and Ti concentrations in the interdendritic zones were slightly higher than those in the dendrite cores. Similar compositional differences in the interdendritic and dendrite cores were observed when viewing the (001) plane of the sample (i.e., viewing in the crystal (dendrite) growth direction).

Direct comparison of hot corrosion in the interdendritic regions and dendrite cores after 5 h is shown in Fig. 9. At every location where the interdendritic regions intersect the surface, and thus interact directly with corrodent, a small upward perturbation was observed in the inner layer. Such regions are indicated by arrows in Fig. 9a and at higher magnification in Fig. 9b. The observations indicate that these regions corroded less than in the dendrite core regions where the γ' precipitates are of smaller volume fraction and size. If preferred reaction with Co is initially driving the formation of the scale, it is not unreasonable to expect that the interdendritic region, containing less Co, would form a thinner scale. In addition, with 12 vol.% more γ' precipitate in the interdendritic regions, less scale formation would be expected, as the γ matrix appears to corrode first based on the observations in Fig. 7. Likewise, the larger cuboids of γ' in the interdendritic regions imply smaller γ channels for the molten liquids to travel through during hot corrosion. Ultimately, further study is required to delineate these mechanisms.

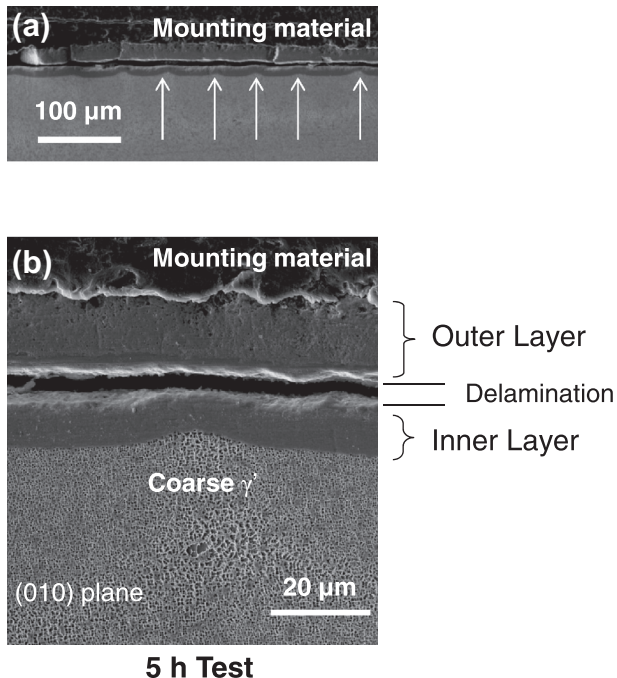


Fig. 9. SEM images showing differences between the hot corrosion of the interdendritic regions and dendrite core regions after 5 h at (a) lower magnification and (b) higher magnification.

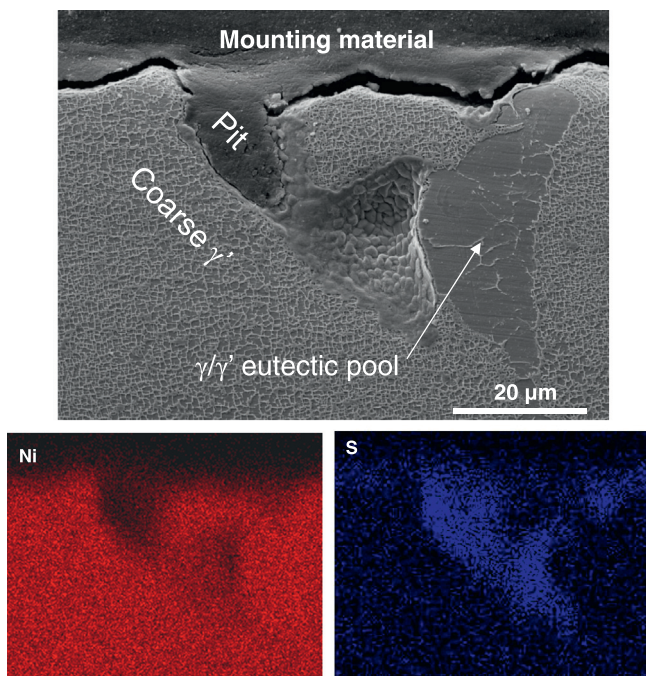


Fig. 10. Typical pit formed at the edge of the interdendritic zone and a γ/γ' eutectic pool after 50 h of Type II hot corrosion. EDS maps show the pit surfaces to be rich in S and devoid of Ni, Cr and Al (not shown) were present in the pit.

Cross-sectional microscopy also revealed corrosion pits, most often associated with small pores in the interdendritic regions (Fig. 10). Stereological measurements indicated ~ 1 pit/cm of line length in the surface after the 5 h corrosion test and ~ 2 pits/cm after the 50 h corrosion test. A pit was classified as local corrosion 2–3 times deeper than the corroded substrate. Pitting was typically

located near the γ/γ' eutectic pools in the interdendritic regions. A high sulfur concentration was normally found inside the pits (Fig. 10), indicating they were open to the surface or near the surface before corrosion started.

3.5. Effect of crystal orientation

There were no differences in surface appearance or cross-section morphology for hot corrosion studies performed on samples oriented such that the (001) plane or (010)=(100) plane was the corroded surface. As determined by XRD, there were no differences in reaction products between the two orientations. Thus, it was concluded that for the experimental conditions of the present study, crystal orientation (transverse or longitudinal to the dendrite growth axis) does not have a significant effect on the Type II hot corrosion mechanism of CMSX-4.

4. Discussion

Based on the experimental results of this study, it is proposed that corrosion of the CMSX-4 occurs in two stages. Stage I is associated with rapid dissolution of the alloy by a molten eutectic of the type $\text{Na}_2\text{SO}_4-\text{MSO}_4$ where M is Ni or Co. Three minutes of testing did not appear long enough to generate substantial conversion of the NiO and CoO into a low-melting temperature eutectic, however 15 min of testing was sufficient to develop inner and outer corrosion layers of combined thickness greater than 10 μm . The Ni- and Co-rich γ matrix appears to be the first phase dissolved by the eutectic, with partial or incomplete dissolving of the γ' precipitates observed (see Fig. 7). The inner layer of the scale appears to be rich in Al, Cr, and S. The exact chemical compounds formed in the inner layer were difficult to assess by XRD, presumably because they were underneath the outer layer. Based on EDS analysis, other alloying elements in the CMSX-4 (e.g., W, Ta, Re) appear to be located in the inner layer as well. The outer layer of the scale is comprised of Ni, Co, O, and S based on detected compounds in the XRD results presented in Fig. 6. Based on all the experimental evidence, stage I is proposed to end when the molten liquid is consumed. XRD results of a specimen corroded for 30 min indicated the presence of NiSO_4 , while XRD results of a specimen corroded for 5 h did not detect this transitory phase. As NiSO_4 is part of the eutectic liquid initially corroding the specimen, this implies stage I ends sometime after 30 min, but before 5 h, for the conditions of this investigation.

In stage II of hot corrosion the flowing $\text{O}_2-\text{SO}_2-\text{SO}_3$ gas in contact with the external surface of the scale formed during stage I sets up a new surface boundary condition. The scale exhibits the formation of oxides and sulfides of Ni, Co, Cr and Al, governed by their interactions with oxygen and sulfur and by their relative interdiffusion behavior through the solid scale. It is worth noting that the equilibrium partial pressures of O_2 , SO_2 , and SO_3 at 700 °C for the gas used in the current study are 0.999 atm, 2.8×10^{-4} atm, and 7.2×10^{-4} atm, respectively [37]. Thus, the predominant gas in the mixture is oxygen. The free energies of formation for Ni, Co, Al, and Cr oxides are more negative than their corresponding sulfides [37]. Thus, it is proposed that in stage II the sulfur-containing phase(s) that formed in the outer layer in stage I, are converted to oxides via a diffusion reaction. Evidence for this reaction is the appearance of NiO and CoO detected by XRD after 30 min and their predominance after 5 h of testing.

In stage II the relative diffusion behavior of the main elements, such as Co and Ni, can be appreciated from an examination of their concentration profiles presented in Fig. 4a and b for the sample tested for 5 h. Based on mass conservation of Co as well as of Ni during the scale growth, the location of the original surface of

the CMSX-4 was calculated and has been marked as x_o at a distance of 8.9 μm from the external surface (x_s), as shown in Fig. 4a and b. The total scale thickness is about 22.3 μm and the interface x_I between the outer and inner layers of the scale is located at 10.6 μm from x_s . For these calculations the molar density, ρ (moles/m³), within the diffusion zone is assumed invariant with time. The interface between the CMSX-4 alloy and the inner layer of the scale is identified at x_{II} . From the concentration profiles of the individual components, profiles of interdiffusion fluxes can be generated on the basis of the relation [38,39]

$$\tilde{J}_i(x) = \frac{1}{2t} \int_{C_i^+}^{C_i(x)} (x - x_o) dC_i \quad (i = \text{Co, Ni, etc.}) \quad (1)$$

where C_i^+ is the initial concentration of the component i in the CMSX-4 exposed to the sulfidizing and/or oxidizing environment. Due to the net mass input of sulfur and oxygen during the growth of the scale, the external surface of the scale/base alloy assembly moves outwards and this motion is assumed to occur parabolically with time with a boundary condition of fixed composition C_s^+ at the external surface. Eq. (1) can then be utilized to calculate interdiffusion fluxes of the individual components within the various layers of the scale and the calculated profiles of interdiffusion fluxes of Co and Ni are presented in Fig. 11a and b. The negative sign for the fluxes, \tilde{J}_i (moles/m² s), in Fig. 11a and b indicates that Co and Ni interdiffuse in the direction from the alloy outwards to the external surface of the scale. These flux calculations are considered approximate, since variations in the molar volumes of the various phases in the scale are ignored and the constancy of boundary conditions for the scale/alloy system is assumed throughout the corrosion test.

The outer layer of the scale in the 5 h sample consisted of mostly mixed oxide (Ni, Co)O. A relative build-up of Co concentration observed in the region of the external surface in Fig. 4a clearly indicates that Co interdiffusing towards the surface exhibits "uphill" interdiffusion up its own concentration gradient. The "uphill" interdiffusion and zero-flux plane phenomena are quite common for individual elements in ternary and multicomponent systems [38] and reflect diffusional interactions among components. The "uphill" interdiffusion of Co ions in the outer layer of the scale occurs down a Ni concentration gradient towards the external surface. On the basis of multicomponent diffusion phenomenology [39,40], this observation implies that the Co interdiffusion is enhanced down a Ni gradient in the (Ni, Co)O outer layer of the scale. Also, Co ions are considered to be more mobile than Ni ions in their oxides, since the concentration of cation vacancies is considered to be higher in CoO than in NiO [20].

Permeation of sulfur through the oxide outer layer of the scale continues to occur in stage II and the S enrichment is mostly observed in the vicinity of the two interfaces, x_I and x_{II} of the scale,

as shown in Fig. 4c. Appreciable enrichment of Cr and Al was also detected by the EDS analysis within the inner layer consisting of the various sulfides and oxides. In the sample tested for 50 h, the inner and outer layers of the scale exhibited evolution of the diffusion structure. The outer layer of the scale included regions of Co-rich oxides distributed within Ni-rich oxide matrix and the inner layer showed bands of enrichment of sulfur adjacent to x_I and x_{II} interfaces, as can be seen in Fig. 5. Such evolution appears to be consistent with observations of compositional distributions (Fig. 4) and flux profiles (Fig. 11) reported for the 5 h sample and needs to be investigated further. Ultimately, the interdiffusion process, as well as the concurrent evolution of the diffusion structure of the corrosion scale in Type II hot corrosion examined in this study, may be better appreciated in the framework of multicomponent diffusion phenomenology on the basis of compositional distributions and interdiffusion flux analysis for various components.

5. Conclusion

An investigation of Type-II hot corrosion of a single crystal Ni-based superalloy (CMSX-4) was conducted, where samples were coated with 0.3 mg/cm² of Na₂SO₄ prior to testing, and heated to 700 °C in an O₂-SO₂-SO₃ atmosphere for times ranging from 3 min to 50 h. Hot corrosion was observed to occur in two stages. Stage I was associated with rapid dissolution of CMSX-4 by a molten eutectic of the type Na₂SO₄-MSO₄, where M is Ni or Co, and ceased after consumption of the applied Na₂SO₄. The corrosion scale developed during stage I consisted of two layers. The outer layer mainly consisted of oxides, sulfates, and possibly sulfides of Co and Ni with an enrichment of Co in the region adjacent to the external surface. The inner layer of the scale, on the other hand, consisted of mixed sulfides of Cr and Al. Microscopic examination of the corroded CMSX-4 alloy indicates that the γ phase corroded relatively faster than the γ' precipitates, as evidenced by residual cuboidal precipitate morphology in the inner layer of the scale.

Stage II began sometime after 30 min, but before 5 h, under the conditions of the present experiments (most notably with the single application of salt). After 5 h, XRD investigations indicated that the nickel sulfate that had formed in stage I had disappeared. The scale formed during stage II was associated with the formation of oxides and sulfides of Ni, Co, Cr and Al and governed by their interactions with oxygen and sulfur and by their relative interdiffusion behavior through the solid scale. The concentration Co is observed to increase towards the external surface of the outer layer. The interdiffusion behavior of Co and Ni in the development of the layers was examined in terms of interdiffusion fluxes. Co exhibits "uphill" interdiffusion up its own concentration gradient towards the external surface in the outer layer of the scale. In terms of diffusional interactions, the interdiffusion of Co ions is enhanced down a Ni concentration gradient. After 50 h, the outer layer exhibits

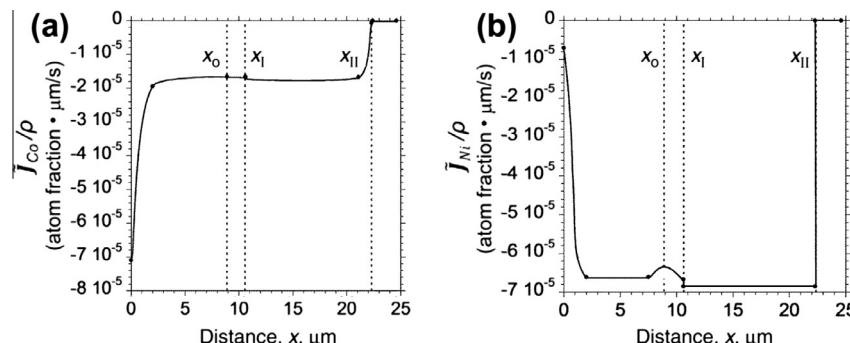


Fig. 11. The calculated Co and Ni flux profiles (a) $\tilde{J}_{\text{Co}}/\rho$ and (b) $\tilde{J}_{\text{Ni}}/\rho$ as functions of distance on the basis of Eq. (1).

Co-rich oxides distributed within the Ni-rich oxide matrix. In the inner layer a relative enrichment of sulfur is observed in the vicinity of the outer layer/inner layer interface as well as at the inner layer/CMSX-4 interface with lower sulfur concentrations observed between these two interfaces.

The bilayer corrosion mechanism characterized in this study does not appear to have been described previously in the literature. Based on the microstructural and microchemical observation of this study on CMSX-4, it should also be operative in other γ/γ' superalloys.

Acknowledgements

The authors wish to thank Alcoa Howmet Research, Whitehall, MI, for providing the slab of CMSX-4 used in the present study. Furthermore, Dr. Lortakul wishes to thank SCG-Chemicals of Thailand for providing the scholarship to obtain a Ph.D. at Purdue University.

References

- [1] D.A. Shifler, High-Temperature Corrosion in Military systems, in: Corrosion: Environments and Industries, ASM Handbook, vol. 13C, ASM International, Materials Park, OH, 2006, pp. 156–170.
- [2] N. Eliaz, G. Shemesh, R.M. Latanision, Hot corrosion in gas turbine components, Eng. Fail. Anal. 9 (2002) 31–43.
- [3] J.M. Gallardo, J.A. Rodriguez, E.J. Herrera, Failure of gas turbine blades, Wear 252 (2002) 264–268.
- [4] Alten F. Grandt Jr., Fundamentals of Structural Integrity: Damage Tolerant Design and Non Destructive Evaluation, Wiley, New York, 2004.
- [5] K.T. Chiang, F.S. Pettit, G.H. Meier, Low temperature hot corrosion, in: R.A. Rapp (Ed.), High Temperature Corrosion, NACE-6, Houston, 1981, pp. 519–530.
- [6] F. Pettit, Hot corrosion of metals and alloys, Oxid. Met. 76 (2011) 1–21.
- [7] K.L. Luthra, Low-temperature hot corrosion of cobalt-base alloys, Part I. morphology of the reaction product, Metall. Trans. 13A (1982) 1843–1852.
- [8] K.L. Luthra, Low-temperature hot corrosion of cobalt-base alloys, Part II. reaction mechanism, Metall. Trans. 13A (1982) 1853–1864.
- [9] J.A. Goebel, F.S. Pettit, Na_2SO_4 -induced accelerated oxidation (hot corrosion) of nickel, Metall. Trans. 1 (1970) 1943–1954.
- [10] G.H. Meier, A review of advances in high-temperature corrosion, Mater. Sci. Eng. A120 (1989) 1–11.
- [11] D. Deb, S.R. Iyer, V.M. Radhakrishnan, A comparative study of oxidation and hot corrosion of a cast nickel base superalloy in different corrosive environments, Mater. Lett. 29 (1996) 19–23.
- [12] R.A. Rapp, Hot corrosion of materials: a fluxing mechanism?, Corros. Sci. 44 (2002) 209–221.
- [13] H. Singh, D. Puri, S. Prakash, An overview of Na_2SO_4 and/or V_2O_5 induced hot corrosion of Fe- and Ni-based superalloys, Rev. Adv. Mater. Sci. 16 (2007) 27–50.
- [14] K.P. Lillerud, P. Kofstad, Sulfate-induced hot corrosion of nickel, Oxid. Met. 21 (1984) 233–270.
- [15] K.L. Luthra, O.H. LeBlanc Jr., Low-temperature hot corrosion of Co-Cr-Al alloys, Mater. Sci. Eng. 87 (1987) 329–335.
- [16] M. Durand-Charre, The Microstructure of Superalloys, CRC Press, Boca Raton, FL, 1997.
- [17] K.A. Bol'shakov, P.I. Fedorov, Fig. 01120-System $\text{Na}_2\text{SO}_4-\text{NiSO}_4$, Zh. Obshch. Khim. 26 (1956) 348–350.
- [18] M.R. Joyce, X. Wu, P.A.S. Reed, The effect of environment and orientation on fatigue crack growth behavior of CMSX-4 nickel base single crystal at 650 °C, Mater. Lett. 58 (2004) 99–103.
- [19] K.A. Bol'shakov, P.I. Fedorov, Fig. 01115-System $\text{Na}_2\text{SO}_4-\text{CoSO}_4$, Zh. Obshch. Khim. 26 (1956) 348–350.
- [20] N. Birks, G.H. Meier, F.S. Pettit, Introduction to the High Temperature Oxidation of Metals, second ed., Cambridge University Press, Cambridge, 2006.
- [21] M.N. Task, B. Gleeson, F.S. Pettit, G.H. Meier, The effect of microstructure on the Type II hot corrosion of Ni-base MCrAlY alloys, Oxid. Met. 80 (2013) 125–146.
- [22] P. Knutsson, H. Lai, K. Stiller, A method for investigation of hot corrosion by gaseous Na_2SO_4 , Corros. Sci. 73 (2013) 230–236.
- [23] K. Zhang, M.M. Liu, S.L. Liu, C. Sun, F.H. Wang, Hot corrosion behavior of a cobalt-base super-alloy K40S with and without NiCrAlYSi coating, Corros. Sci. 53 (2011) 1990–1998.
- [24] J. Ma, S.M. Jiang, J. Gong, C. Sun, Behavior and mechanism of alkali-sulphate-induced hot corrosion on composite coatings at 900 °C, Corros. Sci. 58 (2012) 251–259.
- [25] M. Qiao, C. Zhou, Hot corrosion behavior of Co modified NiAl coating on nickel base superalloys, Corros. Sci. 63 (2012) 239–245.
- [26] W.H. Lee, Oxidation and sulfidation of Ni_3Al , Mater. Chem. Phys. 76 (2002) 26–37.
- [27] W.H. Lee, Hot corrosion mechanism of intermetallic compound Ni_3Al , Mater. Chem. Phys. 77 (2002) 86–96.
- [28] A. Magdziarz, Z. Kalicka, Hot corrosion behavior of Ni_3Al in sulphate-chloride mixture in the atmosphere, Corros. Sci. 49 (2007) 1869–1877.
- [29] M. Levy, R. Huie, F. Pettit, Oxidation and hot corrosion of some advanced superalloys at 1300–2000 °F (704–1093 °C), Corrosion 45 (1989) 661–674.
- [30] M. Li, X. Sun, W. Hu, H. Guan, S. Chen, Hot corrosion of a single crystal Ni-base superalloy by Na-salts at 900 °C, Oxid. Met. 65 (2006) 137–150.
- [31] N.J. Simms, A. Encinas-Opopeza, J.J. Nicholls, Hot corrosion of coated and uncoated single crystal gas turbine materials, Mater. Corros. 59 (2008) 476–483.
- [32] P. Lortakul, Ph.D. Thesis, Purdue University, 2011.
- [33] K.J. Kurzydlowski, B. Ralph, The Quantitative Description of the Microstructure of Material, CRC Press, New York, 1995.
- [34] E.E. Underwood, Quantitative Stereology, Addison Wesley, Reading, MA, 1970.
- [35] NiO: JCPDS 4–835; CoO: JCPDS 43–1004; Co₃O₄: JCPDS 25–1081.
- [36] R.J. Moore, J. White, Equilibrium relationships in the system $\text{NiO}-\text{CoO}-\text{O}_2$, J. Mater. Sci. 9 (1974) 1393–1400.
- [37] O. Kubaschewski, C.B. Alcock, Metallurgical Thermochemistry, fifth ed., Pergamon Press, Oxford, 1979.
- [38] M.A. Dayananda, C.W. Kim, Zero-flux planes and flux reversals in Cu-Ni-Zn diffusion couples, Metall. Trans. 10A (1979) 1333–1339.
- [39] M.A. Dayananda, Diffusion in ternary alloys, in: Bornstein Landolt (Ed.), Diffusion in Solid Metals and Alloys, vol. 26, Springer-Verlag, Berlin, 1990.
- [40] M.A. Dayananda, Diffusion structures and diffusion paths in ternary systems—selected unusual observations, Solid State Phenom. 72 (2000) 123–134.